Insight into the Origin of Ferromagnetism in Fe-Doped ZnO Diluted Magnetic Semiconductor Nanocrystals: An EXFAS Study of Local Structure

Shiv Kumar,[a] **Nidhi Tiwari,**[b] **S. N. Jha,**[b] **S. Chatterjee,**[c] **D. Bhattacharyya,**[b] **N. K. Sahoo**[b] **and Anup K. Ghosh**[*a]

[a]Materials Research Laboratory, Department of Physics, Banaras Hindu University, Varanasi- 221 005, India;

[b]Applied Spectroscopy Division, Bhabha Atomic Research Centre, Mumbai-400085, India;

[c]Department of Physics, Indian Institute of Technology, Banaras Hindu University, Varanasi-221 005, India.

Abstract

In this paper we have studied Structural, local structural and magnetic properties of sol-gel derived $Zn_{1-x}Fe_xO$ ($0 \leq x \leq 0.06$) nanoparticles. The crystalline structure and crystallite size have been estimated by X-ray diffraction with Rietveld refinement and high-resolution transmission electron microscopy (HRTEM). Other structural and local structural properties have been studied by Extended X-ray Absorption Fine Structure (EXAFS)-, X-ray Absorption Near Edge Structure (XANES)- and Raman- analysis. Weak ferromagnetism is observed at room temperature and magnetization increases with increasing Fe-concentration. The oxygen vacancy assisted bound magnetic polarons (BMPs) and may be the grain boundaries are responsible for this room temperature ferromagnetism. Variation of resistivity with temperature has also been studied. Appearance of ferromagnetism in ZnO:Fe nanoparticles may open the potential in bio-imaging and drug-delivery applications.

* Corresponding author: akghosh@bhu.ac.in; anupkg66@gmail.com

Introduction

Ferromagnetic ordering at room temperature in diluted magnetic semiconductors (DMSs)[1] have recently attracted great interest for their promising applications in the field of spintronics and many other spin-based devices.[2,3] Although, a few devices based on GMR in ferromagnetic/non-magnetic/ferromagnetic type hetero-structures have been successfully fabricated, the major success of spintronics is still waiting for the development of the DMSs.[2,3] Doping of wide band-gap semiconductors with transition metal (TM) elements such as Mn, Fe, Co, etc. gives an effective mean of tuning both the ferromagnetism[4–8] and the optical properties.[9–12] Hence both the charge and spin of electrons can be utilized for devices such as light emitting devices, spin field-effect transistors and spin based quantum computers etc**.** Moreover, the ability of tailoring the physical properties of nanocrystals (NCs) by changing their size and surface functionality produces NCs an attractive building block for functional devices. Again, the principal requirement for realization of spintronic devices depends on the development of DMSs with ferromagnetism at room temperature (RTFM) or above ambient temperature.[2,3] Therefore, much efforts have been paid to make TM-doped wide band gap DMSs nanostructures those exhibit ferromagnetic ordering above room temperature, high mobility and charge carrier concentration for spin-based applications.[13,14]

Zinc oxide (ZnO) is a wide direct band gap ($E_g{\sim}3.37$ eV) II–VI semiconductor with hexagonal wurtzite structure of C^4_{6v} (P6$_3$mc) space group. ZnO has been identified as a promising host material after theoretical prediction for potential ferromagnetism above room temperature in several TM doped ZnO-based DMSs.[15,16] Thereafter, quite controversial results on TM- doped ZnO have been reported.[16–19] For examples, Tamura et al.[17] got RTFM in Fe-doped ZnO thin film while not for Mn- and Co-doped ZnO. Singhal et al. reported weak ferromagnetism at room temperature in colloidal Fe-doped ZnO nanocrystals and described that as an intrinsic property.[18] Kumar et al. also have shown weak ferromagnetism at room temperature in polycrystalline Fe-doped ZnO nanorods.[19] On the other hand, Mishra et al.[20] reported the weak ferromagnetism at room temperature in Fe doped ZnO nanocrystals and Zn-vacancy was taken to be responsible behind the ferromagnetic order. In some recent studies,[21] magnetic anisotropy of the dopant cation has

been proposed to be a signature of intrinsic ferromagnetism in dilute magnetic oxide materials.

Therefore, discrepancies in the experimental results for the same DMS materials prepared by different methods and/ or by different researcher groups have created doubts about the origin of ferromagnetism in these materials. Hence, although there is significant progress and exciting experimental data, the origin of ferromagnetic ordering in DMS nanostructures remain poorly understood. The doping concentrations in DMSs are usually well below the percolation limit to explain on the basis of double-exchange or super-exchange interaction which are used for magnetic interactions in oxides.[22] Very recently, Straumal et $al.$ showed that the grain boundary (GB) and hence grain boundary specific area (S_{GB}) is one of the controlling factors for the ferromagnetic behavior of undoped and TM-doped ZnO.[23,24] Again, Kumar et $al.$[8] observed room temperature weak ferromagnetism in Co doped system in which the joint effects of grain boundaries, oxygen vacancy and bound magnetic polarons (BMPs) were considered for room temperature ferromagnetism (RTFM). Hence, magnetism in Fe-doped ZnO nanoparticles is an interesting and controversial issue to be solved. Moreover, to insight into the origin of ferromagnetic ordering, local structure around Zn atoms in Fe- doped ZnO nanocrystals has been studied by EXAFS and X-ray Absorption Near Edge Structure (XANES) measurements.

On the other hand, magnetic- and DMS- nanoparticles, due to their unique physical (viz. luminescent and magnetic properties) and chemical properties, have many advantages in biomedical applications, such as contrast agents for bio-imaging, as colloidal mediators for magnetic hyperthermia or as active constituents of drug-delivery platform.[25–27] These unique properties are based on their similarity in size with bio-molecules, large surface areas, and quantum size effects. ZnO nanoparticles have shown promising potential in biomedical applications such as bio-imaging and drug delivery.[27] Appearance of ferromagnetism in ZnO:Fe nanoparticles opens the potential in bio-imaging applications. In a well-planned in vivo experiment, the nanocomposites of ZnO nanoparticles loaded with drugs or ZnO hollow spheres containing drugs are injected into a mouse[27] and nanocomposites were able to penetrate cancer cells. Since the tumor and cancer cells have acidic environments in lysosomes and endosomes, the ZnO nanocomposites were decomposed and released the drugs. This process was detected by magnetic resonance

imaging (MRI). Considering their wide range of applications, the impact of ZnO and Fe-doped ZnO nanomaterials on human health and the environment is of great interest.

In this paper we have studied on the structural, local-structural, optical, and magnetic properties of Fe-doped ZnO (i.e. $Zn_{1-x}Fe_xO$) nanocrystals to get a clear understanding of the origin of ferromagnetic ordering for the application in biomedical imaging.

Experimental details

$Zn_{1-x}Fe_xO$ ($0 \leq x \leq 0.06$) samples (named Fe0, Fe0.5, Fe1, Fe1.5, Fe2, Fe4, and Fe6 for Fe-concentration x = 0, 0.005, 0.01, 0.015, 0.02, 0.04, and 0.06 respectively) have been synthesized by the sol-gel method. Appropriate proportions of analytical grade metal nitrates $Zn(NO_3)_2 \cdot 6H_2O$ (purity ~99.9%) and $Fe(NO_3)_3 \cdot 9H_2O$ (purity ~99.9%) powders were thoroughly mixed. With stirring the mixture was dissolved in aqueous solution of citric acid [$C_6H_8O_7$] (purity ~99.6%) to obtain a homogeneous precursor solution. The citric acid acts as a fuel for the reaction. The precursor solution was dried at 80 °C for 3h to obtain a xerogel and the swelled xerogel was kept at 130 °C for 12 h. The simplified exothermic reaction can be expressed as:

$$M(NO_3)_2 + C_6H_8O_7 + 4O_2 \rightarrow MO + 2NO_2 + 6CO_2 + 4H_2O; (M = Zn, Fe).$$
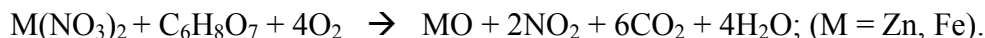
After grinding, the xerogel powders were sintered at 600° C for 10 h in air atmosphere to get $Zn_{1-x}Fe_xO$ nanoparticles.

Structural characterization of $Zn_{1-x}Fe_xO$ samples was performed by X-ray diffractometer (Model: Miniflex-II, Rigaku, Japan) with Cu Kα radiation (λ = 1.5406 Å). The EXAFS measurements have been carried out at the Raja Ramanna Centre for Advanced Technology (RRCAT), Indore, India with the dispersive EXAFS beamline (BL-8) at the INDUS-2 Synchrotron Source (2.5 GeV, 120 mA). Above beam line uses a 460 mm long Si (111) crystal mounted on a mechanical crystal bender that can bend the crystal to the shape of an ellipse. The crystal selects a particular band of energy from white synchrotron radiation depending on the grazing angle of incidence (Bragg angle) and disperses as well as focuses the beam on the sample. The beam line has a resolution of 1 eV at the photon energy of 10 keV. For getting a reasonable edge jump, appropriate weights of the powdered sample have been mixed thoroughly with cellulose powder (to get a total weight of

4

approximately 150 mg so that 2.5 mm thick homogenous pellets of 12.5 mm diameter were made). TEM and HRTEM measurements were done with Technai G^2 S-Twin (FEI, Netherlands). Fourier transmission infrared (FT-IR) spectra of the samples (as pellets with KBr) were obtained using FT-IR Spectrometer (Spectrum One, Perkin Elmer Instrument, USA) in the range of 400–4000 cm^{-1} with a resolution of 1 cm^{-1}. Raman spectra were taken with a Reinshaw micro-Raman spectroscope in the range of 200–1250 cm^{-1} using 514.5 nm Ar$^+$ laser as excitation source. The powder samples are made into pellets for the Raman measurements.

The D.C magnetization (M-H) measurements have been carried out by a Physical Properties Measurement System (PPMS) of Cryogenics Inc, USA and by a Vibrating Sample magnetometer (VSM) from Lakeshore (Model no: 7407). The resistivity measurements were carried out by the conventional two-probe method fitted with a Closed Cycle Cryo-cooler.

Results and discussions

Structure and composition
X-ray Diffraction

Rietveld refinement of the X-ray diffraction (XRD) patterns for Zn$_{1-x}$Fe$_x$O (0≤x≤0.06) samples are shown in Fig. 1. All peak positions of Fe-doped ZnO correspond to the standard Bragg positions of hexagonal wurtzite ZnO (space group *P6$_3$mc*) have been shown by the vertical bars and the residue by the curved line respectively at the bottom of the XRD patterns. Figure 1 shows that the Fe-doping causes to create no extra peak or disappearance of any peak of the hexagonal wurtzite structure of pure ZnO. It confirms that the structure of the doped ZnO remains wurtzite phase belonging to the space group *P6$_3$mc*. Thus, the Rietveld analysis shows that the samples are of single phase and no trace of other impurities has been found. All the XRD peaks have been indexed using the standard JCPDS file for ZnO (JCPDS #36–1451).

From Rietveld refinement of the X-ray diffraction data, the lattice parameters ('*a*' and '*c*') have been measured and their variation with Fe-concentration (x) is shown in Fig. 2. The volume of the unit cell for a hexagonal system has been calculated from the equation:[28]

$$V = 0.866 \times a^2 \times c \qquad\qquad (1)$$

Variation of the unit cell volume with Fe-concentration calculated from eqn.1 is shown in the inset (i) of Fig. 2. The figure reveals that there is small increase in the lattice parameters '*a*' and '*c*' and the volume of the unit cell due to increase of Fe-ion doping. This result is similar to the previous observations.[29–32] Moreover, FT-IR study[9] confirms that Fe-ions doesn't enter into the octahedral coordination (as discussed latter). To explain small increment of lattice parameters '*a*' and '*c*' and unit cell volume (V), we have considered the distortion of Zn tetrahedron[33, 34] due to Fe-doping. In an ideal wurtzite structure there are two interpenetrating hexagonal-close-packed (*hcp*) sub-lattices with two lattice parameters, *a* and *c*, in the ratio of $c/a = \sqrt{(8/3)}$. Again, *a/c* is the measure of the distortion from its ideal tetrahedron and the degree of distortion *R= [$\sqrt{(8/3)}$ (a/c)]* where *R=1* gives the ideal wurtzite structure [35] with $c/a = \sqrt{(8/3)}$. In a real ZnO crystal, the wurtzite structure deviates from the ideal arrangement, by changing the *a/c* ratio or the *R* value. The variation of the degree of distortion *R* is shown in the inset (ii) of Fig. 2. In wurtzite ZnO, the Zn-tetrahedron has the base in the *ab*-plane and the apex along the *c*-direction. Different parameters such as *a*, *c*, *c/a,* bond lengths, bond angles, etc. have been calculated from Rietveld refinement and following Morkoc and Özgür [33,34,] (Table 1). Variations of bond angles and bond lengths with Fe-concentration are shown in Fig. 3 (a) and 3(b) respectively. From Fig. 3(a) it has been observed that the average basal bond angles (O_b-Zn-O_b) and average base-apex angles (O_b-Zn-O_a) [where O_b and O_a are oxygen atoms at the base and at the apex of the tetrahedron respectively] are constant with Fe-doping. However, both the bond length of Zn-O_a and Zn-O_b bonds increase slowly [Fig. 3 (b)] giving rise to the slow increase of the lattice parameters *a* and *c*. The increase in Zn-O bond lengths have also been observed by EXAFS measurements (discussed latter) and have been attributed to the substitution of Zn^{+2} ions (ionic radius 0.60 Å) by Fe^{+3} ions of smaller size (ionic radius 0.49 Å), as confirmed by XANES measurement. The degree of distortion *R* [inset (ii) of Fig. 2] remains constant with Fe-concentration suggests that both the parameters *a* and *c* varies with the same manner with Fe-concentration. The linear increase of the unit cell volume (V) has been justified by quadratic increase of '*a*'. Again, linear variation of lattice constants '*a*' and '*c*' with increasing Fe-concentration confirms that the doping of Fe- ions does not

change the wurtzite structure (space group $P6_{3mc}$) of ZnO and Fe-ion has been substituted into the crystal lattice following the Vegard's law.[36] Variations of interplanar spacing (d-value) of (100) plane with increasing Fe-concentration are plotted in the inset of Fig. 3(b) which shows that d-value of (100) plane decreases with increasing Fe-concentration. This observation can be explained with the change of the bond lengths. The variation of bond lengths develops the lattice strain.[28] This lattice strain changes the d-spacing (spacing of crystallographic planes). The Bragg angle should either decrease or increase when d-spacing changes. Thus, uniform compressive strain with decreasing the d- spacing shifts a Bragg's peak to higher 2θ value, whereas the uniform tensile strain with increasing the d- spacing shifts a Bragg's peak to lower 2θ value in the spectrum. Since the d-spacing for the (100) plane is decreased with Fe-concentration, [inset of Fig. 3(b)] we say that a uniform compressive strain (hence stress) has been developed in the perpendicular direction of the plane (100). The crystallite size and lattice strain developed in different samples have been estimated from Williamson–Hall (W–H) plot[37] (see Table 2). A better estimation of the size and strain parameters has been obtained from 'size-strain plot' (SSP)[38] by using the following equation:

$$\left(\frac{d_{hkl}\beta Cos\theta}{\lambda}\right)^2 = \frac{k\lambda}{D}\left(\frac{d_{hkl}^2\beta Cos\theta}{\lambda^2}\right) + \left(\frac{\varepsilon}{2}\right)^2 \tag{2}$$

where, d_{hkl} is the interplaner spacing and ε is the average strain produced in the lattice, λ is the wavelength of radiation used (λ =1.5406 Å), θ is the Bragg angle and β is the full width at half maximum (FWHM), D is the average crystallite size and k is the Scherrer constant (= 0.9). The plot of $(d_{hkl}\beta Cos\theta/\lambda)^2$ vs. $(d_{hkl}^2\beta Cos\theta/\lambda^2)$ is shown in Fig. 4. The crystallite size (D) and average strain (ε) have been estimated from the slope and the intercept of the linear fit of the plot respectively (see Table 2). Figure 5 shows the variation of crystallite size (D) and inset of Fig. 5 shows the variation of average strain (ε) with x estimated from size-strain plot. It has been observed that the average crystallite size decreases with the increase of Fe-concentration. This result is consistent with the observation of Mishra et al.[20] However, it reported the qualitative decrement of the crystallite size where as we have observed an exponential decay which is consistent with our earlier report[9] calculated from Debye–Scherrer's equation. This is may be because of incorporation of smaller size cation (Fe^{+3}) in ZnO lattice. Thus different trends in particle

size and lattice constant may be attributed to the intra and inter nucleating forces forming the nanocrystals.[11]

Transmission Electron Microscopy

The morphology and the microstructure of nanoparticles have been examined by transmission electron microscopy (TEM). Typical TEM, HRTEM and SEAD images of Fe0 (pure ZnO) and Fe2 nanoparticles are presented in Fig. 6 (a) - (d). Fig.s 6(a) and 6(d) represents the TEM images of Fe0 and Fe2 nanoparticles respectively. These images show that the nanoparticles tend to coalesce into aggregate which is usually common in magnetic nanoparticles. Closer observations of TEM images of different parts of the sample show that most nanoparticles are more or less spherical in shape having smooth surfaces. These nanoparticles contain very developed grain boundaries and free surfaces which may affect the physical properties as reported by Straumal *et al*.[23,24] The average crystallite size obtained from TEM measurements corroborate with the value estimated from the XRD study. The HRTEM micrographs of a single crystallite of Fe0 and Fe2 nanoparticles (Fig. 6(b) and 6(e) respectively) show that the *d*-value is 0.280 nm and 0.274 nm for Fe0 and Fe2 respectively which is in good agreement with that of (100) plane (viz. 0.281 nm) of wurtzite ZnO. Moreover, it should be pointed out here that the *d*-value of Fe2 (determined from TEM measurements) has also decreased which corroborates the XRD analysis (the compressive strain has been induced due to Fe-doping in the system). The HRTEM pattern also indicates that all the nanoparticles are single crystalline in nature and are free from major lattice defects. The selected area electron diffraction (SAED) pattern (Fig. 6(c) and 6(f) for Fe0 and Fe2 respectively) also shows the single crystalline nature of the samples. According to the results of XRD pattern and HRTEM images, we say that the Fe-ions have been well incorporated into the crystal lattice of ZnO.

EXAFS at Zn K-edge

In the EXAFS experiments the bent crystal selects particular band of energy from white synchrotron radiation depending on the grazing angle of incidence (Bragg angle) of the synchrotron beam and disperses as well as focuses the beam on the sample.[39,40] In EXAFS measurement, the plot of absorption versus photon energy is obtained by recording

the intensities I_t and I_0 on the CCD, with and without the sample respectively and using the relation, $I_t = I_0 e^{-\mu t}$ where μ is the absorption coefficient and t is the thickness of the absorber. In the present experiment the crystal has been set at the proper Bragg angle such that a band of energy obtained around Zn K edge is ~ 9659 eV. For calibration of the CCD channels at the Zn K edge, EXAFS spectra of standard metal foils of Zn and Ga have been used, assuming the theoretical values[41] of Zn K-edge of 9659 eV and Ga K Edge of 10367 eV. Figure 7 represents the experimental EXAFS ($\mu(E)$ versus E) spectra of Fe doped ZnO NCs at Zn K-edge.

The radial distribution function or the the $\chi(R)$ vs. R (or FT-EXAFS) spectra in terms of the real distances from the center of the absorbing atom have been generated from the $\mu(E)$ versus E spectra following the standard procedures[42]. A set of EXAFS data analysis program (available within the IFEFFIT software package) have been used for reduction and fitting of the experimental EXAFS data.[43] This includes data reduction and Fourier transform to derive the $\chi(R)$ vs. R spectra from the absorption spectra (using ATHENA software), generation of the theoretical EXAFS spectra starting from an assumed crystallographic structure and finally fitting of the experimental data with the theoretical spectra using the FEFF 6.0 code (using ARTEMIS software). The bond distances, co-ordination numbers (including scattering amplitudes) and disorder (Debye-Waller) factors (σ^2) which give the mean square fluctuations in the distances, have been used as fitting parameters. It should be mentioned here that the passive electron reduction factor (S_0^2 value) obtained by fitting the FT-EXAFS spectrum of the undoped ZnO sample has been used in case of fitting the spectra of the Fe doped samples.

Figure 8 shows the FT-EXAFS [$\chi(R)$ vs. R] spectra of undoped and Fe doped ZnO samples at the Zn K edge with the best fit theoretical spectra. The theoretical FT-EXAFS spectra have been generated assuming the model described by Kisi et al.[44] namely the first oxygen shell (Zn-O1) at 1.98 Å with coordination number (CN) of 3, second oxyg en shell (Zn-O2) at 1.99 Å having CN of 1 and a Zn shell (Zn-Zn) at 3.21 Å with a CN of 12 in order to fit the first few peaks (in the k range of 3-10 Å^{-1} and upto 3.5 Å in R space) obtained in the $\chi(R)$ versus R spectra of the samples. The variation in average bond lengths of the first two Zn-O shells and the bond length of the Zn-Zn shell along with the uncertainties

involved in the estimation is shown in Fig. 9, while total coordination numbers of the two Zn-O shells and coordination number of the Zn-Zn shell is shown in Fig. 10. Average Debye-Waller factors (σ^2) of the first two Zn-O shells and that of the Zn-Zn shell is shown in Fig. 11 as a function of Fe doping concentration. From Fig. 9 it is observed that up to 1% Fe doping, Zn-O bond lengths increase with increase in Fe doping concentration. This corroborates with the Fe K edge XANES results (given below) which shows that Fe^{+3} substitutes Zn^{+2} in ZnO lattice and since ionic radius of Fe^{+3} (0.49 Å) is less than Zn^{+2} (0.60 Å), Fe atoms substituted in Zn sites attract oxygen atoms closer resulting in elongation of Zn-O bond lengths. Similar changes in bond lengths due to doping have been observed in many cases, for example in case Mn doped ZnO by Basu et al [45] and in Zr doped TiO_2 samples observed by Lippens et al.[46] which were explained on the basis of difference in ionic radius. Also substitution of Fe atoms in Fe^{+3} states increases oxygen coordination in the neighborhood of Fe atoms to establish charge balance. This leads to reduction of oxygen coordination in the neighborhood of Zn atoms manifesting the presence of oxygen vacancies in the sample which increases with increase in Fe doping concentration as shown in Fig. 10. It is corroborated with our earlier result that for dopant with lower ionic radius, oxygen vacancies are created near the host site i.e. in the neighborhood of Zn. However, Zn-Zn bonds remain almost unaltered due to low values of doping. It should also be noted that for more than 1% Fe doping, Zn sites get distorted significantly as manifested by the steep increase in Debye-Waller factor at Zn sites as shown in Fig. 11. It also corroborates by the fact that for more than 1% Fe doping, Zn-Zn bond length decreases significantly.

XANES measurements at Fe K-edge

Figure 12 shows the X-ray Absorption Near Edge Structure (XANES) spectra at the Fe edge of the samples along with Fe metal foil and a standard sample of FeO and Fe_2O_3 where Fe is in 0, +2 and +3 oxidation states respectively. The results of the XANES measurements have been shown for all samples of Fe doping (0.5%, 1%, 4% and 6%) covering the full concentration range along with those of the standards. It has been observed that for all the samples the Fe K-edge position matches with that of the Fe_2O_3 standard sample which indicates that Fe exists in the Fe^{+3} state. However, it can also be seen that the absorption edge of Fe in the samples does not resemble the sharp white line of standard

Fe_2O_3 sample, rather they are shallow, indicates that Fe does not exist as a separate Fe_2O_3 phase in ZnO, rather Fe exists as Fe^{+3} in the ZnO lattice. Thus the XANES study clearly rules out the presence of Fe metallic clusters, FeO and Fe_2O_3 in the samples and indicates substitution of Zn^{+2} with Fe^{+3} in the tetrahedral lattice.

Raman Spectroscopy

Raman spectroscopy is one of the most powerful nondestructive techniques to study the structural disorder, crystalline quality, and defects in the host lattice.[47] It has been employed to examine the crystalline quality of $Zn_{1-x}Fe_xO$ nanoparticles. Wurtzite ZnO belongs to the C^4_{6v} symmetry group and has a total number of 12 phonon modes namely: one longitudinal-acoustic (LA), two transverse-acoustic (TA), three longitudinal-optical (LO), and six transverse-optical (TO) branches. At the Γ point of the Brillouin zone, optical phonons have the irreducible representation [48] as: $Γ_{opt} = A_1 + 2B_1 + E_1 + 2E_2$, where both A_1 and E_1 mode are polar and can be split into transverse optical (TO) and longitudinal optical (LO) phonons, with all being the Raman and infrared active. Non-polar E_2 modes are Raman active, while B_1 modes are Raman inactive. The vibration of heavy Zn sublattice gives rise to the low-frequency E_2 mode while that of oxygen sublattice gives rise to high-frequency E_2 mode.[49] Modes E_1 (TO) and A_1 (TO) reflect the strength of the polar lattice bonds.[50] In the unpolarized Raman spectra of bulk ZnO under backscattering geometry, according to the selection rule only E_2 and A_1 (LO) modes can be observed. However, when the crystal is reduced to nanometer size, the selection rule with k=0 for the first-order Raman scattering is relaxed and phonon scattering is not being limited to the center of Brillouin zone, [48] the phonon dispersion around the zone center should also be considered in that case. Therefore, not only the first-order vibration modes should appear with shift and broadening but also some vibration modes may exist from the symmetry-forbidden geometries. As a result, six Raman-active phonon modes at 101cm^{-1} (E_2 low), 381 cm^{-1} (A_1 TO), 407 cm^{-1} (E_1 TO), 437 cm^{-1} (E_2 high viz. E_{2H}), 574 cm^{-1} (A_1 LO), and 583 cm^{-1} (E_1 LO) have reported for the wurtzite ZnO nanoparticles.[51, 52] Figure 13 represents the room-temperature Raman spectra of $Zn_{1-x}Fe_xO$ (0≤x ≤0.06) nanocrystals. Though, due to the limitation of the experimental set-up, the phonon mode at 101 cm^{-1} (E_2 low) has not been observed, all other prominent

11

peaks have been observed very clearly for ZnO and Fe-doped ZnO nanocrystals. The assignments of the Raman modes of $Zn_{1-x}Fe_xO$ nanoparticles obtained for different Fe-concentration (x) are summarized in Table 3. The sharpest and strongest peak at about 434 cm^{-1} can be assigned as the nonpolar high-frequency optical phonon branch of E_2 mode (E_{2H}), which involves the motion of oxygen and is also the characteristic of wurtzite structure. With increasing Fe-concentration, pronounced weakening in peak height of this E_{2H} mode has been observed without any appreciable shifting and broadening in frequency of this mode. To estimate this variation with Fe-concentration, intensity ratio of $(E_{2H})_x/(E_{2H})_0$ [where $(E_{2H})_x$ and $(E_{2H})_0$ are the intensity of E_{2H} modes for Fe-concentration (x) and pure ZnO respectively] has been calculated and plotted in the inset of Fig. 13. The intensity ratio of $(E_{2H})_x/(E_{2H})_0$ decreases linearly (see inset of Fig. 13) with increasing Fe-concentration (x). This result can be attributed to the fact that Fe^{2+} substitution induces the microscopic structural disorder in the periodic zinc sublattice and reduces the translational symmetry giving rise to local distortions in the lattice. This local distortion and disorder disrupts the long-range ordering in ZnO and weakens the electric field associated with the mode.[52] In other words, this observation reveals that the local symmetry in the nanocrystals is different from that of undoped sample (i.e. ZnO), but the crystal structure remains the same. Closer observation shows two very weak peaks at 408 cm^{-1} [E_1 (TO) mode] and 585 cm^{-1} [E_1 (LO) mode] in pure ZnO only and they are disappeared for all the other samples. This may be due to local distortions in the lattice of the doped samples. The peak at about 329 cm^{-1} and a broad shoulder centered at about 658 cm^{-1} for ZnO (Fig. 13) seemed to have originated from a two-phonon process.[53] The peak at about 329 cm^{-1} can be attributed to single crystalline nature of ZnO[50, 51] and assigned as a difference mode between the E_2 high and E_2 low frequencies[54, 55] viz. $(E_{2H} - E_{2L})$. The peak height and frequency of this peak remains unaffected with Fe-doping concentration (Fig. 13). This suggests that the single crystalline nature remains unchanged due to Fe-doping and it corroborates the TEM observations. The mode at 658 cm^{-1} in pure ZnO nanostructure can be ascribed to the 2nd order mode [viz. $2(E_{2H}-E_{2L})$] of $(E_{2H}-E_{2L})$ arise due to multi-phonon processes.[56, 57] For Fe-doped ZnO samples, this peak (at 658 cm^{-1} in pure ZnO) remains constant till x=0.04 but shifted to 680 cm^{-1} for x=0.06 sample. Comparing Fig. 13, it has also been observed that the shoulder centered at about 658 cm^{-1} gradually becomes a peak by increasing its intensity

with increasing Fe-concentration. The increment of this peak (2nd order mode) has been quantified by taking the ratio of the intensity of $2(E_{2H}–E_{2L})$ peak to that of $(E_{2H}–E_{2L})$ and the behavior has been plotted in the inset of Fig. 13. Other 2nd order mode at around 1142 cm^{-1} [$2A_1(LO)$] for ZnO remains unshifted with increasing Fe- concentration. It should be noted here that the 2nd order mode has been assigned whose frequency is nearly double of any 1st order mode. The weak mode A_1 (TO) at 378 cm^{-1} for ZnO remains unchanged for the samples up to x=0.04 and the mode has been shifted to the lower frequency ~354 cm^{-1} and called as NM for the sample x=0.06 (which does not appear in Raman spectrum for Fe0 to Fe4). Ye et al.[58] considered two possible mechanisms to ascribe the origin of this anomalous mode: disorder-activated Raman scattering (DARS) and local vibrational modes (LVMs). The DARS was said to be induced by reducing the translation symmetry of the lattice caused by defects or impurities due to the nature of the dopant or due to the growth conditions. Therefore, it can be presumed that NM in our samples could arise due to either or both of these two mechanisms. The mode at 547 cm^{-1} can be assigned to the quasi-longitudinal-optical (LO) phonon mode, [48] due to the shallow donor defects, such as zinc interstitials and/or oxygen vacancies, bound on the tetrahedral Fe- sites. Hence, in $Zn_{1–x}Fe_xO$ nanocrystals host Zn ions are partially substituted by Fe-ions, introduces lattice defects and disorder in host ZnO crystals disturbing the long range ionic ordering in the ZnO.

FT-IR Spectroscopy

The study on Fourier transform infrared spectroscopy (FT-IR) of this system[9] has reported earlier.[9] Here we have analyzed those data. The result reviles that the tetrahedral co-ordination (peak at around 480 cm^{-1}) is much stronger than the octahedral co-ordination (peak at around 660 cm^{-1}). Closer observation [9] shows that the (negligibly weak) band at around 660 cm^{-1} due to octahedral co-ordinations remains unaffected for Fe-doping. This result suggests that Fe-ions does not enter in the octahedron but enter in the tetrahedron only.

Magnetization

We have conducted a detailed study on the RT magnetization of $Zn_{1-x}Fe_xO$. M-H curve of some of the samples are plotted in Fig. 14. The magnetization decreases with the increase in the field for Fe0 and Fe2 whereas it increases with the increase in the magnetic field for Fe4 and Fe6. The observed M-H behavior reveal that the samples Fe0 and Fe2 is a mixture of ferromagnetic (FM) and diamagnetic (DM) phases where DM dominates. The sample Fe4 and Fe6 are in weak ferromagnetic. As seen in Fig. 14, the sample Fe4 has a well defined hysteresis loop even at room temperature with a coercive field of 0.07 T and a remnant magnetization of 0.005 emu/g. The obtained hysteresis at room temperature supports the fact that the sample is weakly ferromagnetic[18–20,30] and not superparamagnetic.[59, 60] Thus, the magnetization increases with increasing Fe-concentration and weak ferromagnetism arises gradually.

To investigate the origin of RT-ferromagnetism (FM) in Fe-doped ZnO, several mechanisms proposed in the literature have been considered viz. (i) the possibility of spurious ferromagnetism due to magnetic impurities as the intrinsic property of the doped NPs, (ii) extended defects in the NPs, (iii) formation of some Fe-related nanoscale secondary phase, (iv) metallic iron precipitation, and (v) formation of FeO/ Fe_2O_3. However, contributions of FeO/ Fe_2O_3 phases can be ruled out because presence of separate FeO/ Fe_2O_3 phase was not found in the samples with XRD, EXAFS, and TEM measurements. Secondly, metallic Fe clusters and Fe-related secondary phases are also unlike source of this FM because of XRD, EXAFS, and HRTEM results. Since in the present case, undoped ZnO prepared under identical conditions as those of Fe-doped ZnO samples, does not exhibit any measurable ferromagnetism but shows diamagnetism, impurities cannot contribute to the observed magnetic moment in the Fe-doped ZnO NPs. Thus, TMs essentially plays the key role to the observed FM. Again, recently Straumal et $al.$ showed that the grain boundary specific area (the ratio of the grain boundary area to the volume) S_{GB}, is the controlling factor for the ferromagnetic behavior of undoped and TM-doped ZnO.[23, 24] For Fe-doped ZnO nanocrystals Straumal et al. [61] argued that the samples are FM only if S_{GB} exceeds a certain threshold value $S_{th} = 3 \times 10^4$ m^2/m^3. For our system S_{GB} value is well above the threshold value viz. $S_{GB} = 41 \times 10^6$ m^2/m^3) giving the FM. Hence, FM is expected to arise due to the joint effects of the intrinsic exchange interaction of magnetic moments of TM ions and effects of the grain boundary in doped NPs.

However, the exact mechanism of intrinsic FM in TM-doped oxides is still controversial.[11,21] Number of diverse theories have been proposed, such as (I) the localized magnetic moments are assumed to interact with each other via carrier (free electron)-mediated Ruderman–Kittel–Kasuya–Yosida (RKKY)- type interactions, (II) the mean-field Zener Model,[15] (III) the double exchange (direct interaction) mechanism[16] or superexchange mechanism (indirect interaction). In double exchange mechanism magnetic ions in different charge states (d states of TM ions) couple with each other by virtual hopping of the extra electron from one ion to the other through interaction with p-orbitals. Superexchange mechanism is an indirect exchange interaction between non-neighboring magnetic ions which is mediated by a non-magnetic ion which is placed in between the magnetic ions. (IV) the donor impurity band exchange model, where the FM in DMSs is accounted for by an indirect exchange via shallow donor electrons that form bound magnetic polarons (BMP). [62-64]

Since the RKKY interaction is based on free electrons and ZnO is not transformed into a metal with such a low doping (confirmed by electrical resistivity measurements discussed in the next Sec.), RKKY interaction is not valid here. Double-exchange or superexchange are not responsible for the FM because the magnetic cations are dilute (of low concentration) in the present samples. However, according to donor impurity band exchange model the combination of magnetic cations, carriers, and defects can result in bound magnetic polarons (BMPs) which may also lead to the RTFM. [62-64] From the XANES and EXAFS results described above it has been found that oxygen vacancies are present in the samples which increases with increase in Fe doping concentration. Thus, we think that oxygen vacancy assisted BMPs contribute to the RTFM in this system.[62-65] Similar results have also been observed in case of Co doped ZnO samples.[8] Therefore, we suggest that the joint effects of the intrinsic exchange interactions arising from the oxygen vacancy assisted bound magnetic polarons (BMPs) and the (extrinsic) grain boundary are responsible for the room temperature FM in this system.

Electronic transport properties

Temperature variation of electrical resistivity (ρ) of Fe-doped ZnO samples has been measured to see the effect Fe-doping on the electrical conduction. The results have been shown in Fig. 15. The exponential decrease in resistivity with increasing temperature tells that Fe-doped ZnO samples maintain the semiconducting nature for all Fe-concentrations as that of undoped ZnO. This observation rules out the possibility of $Zn_{1-x}Fe_xO$ to become metallic due to Fe-doping. This result corroborates the result of XANES study. The plot of *ln*ρ *vs.* 1000/T (Inset (i) of Fig. 15) shows two different slopes in the low and high temperature regions which is the signature of two different conduction mechanisms being active in these two temperature regions. The liner fit shows that thermally activated band conduction is the dominant mechanism at high-temperature region. The thermally activated resistivity at high temperature region follows the Arrhenius law:

$$\rho(T) = \rho_0 \exp[E_a / k_B T] \qquad (5)$$

where k_B is the Boltzmann's constant and E_a is the activation energy. The activation energy (E_a) for the samples has been calculated using Arrhenius law (Eqn. 5) and values are given in Table 5.

The deviation from the linear fit of *ln*ρ *vs.* 1000/T plot (Inset (i) of Fig. 15) indicates that thermal activation mechanism is not valid at low temperature region. The variable-range-hopping (VRH) conduction of polarons has been found to dominate in this low temperature region. The conduction mechanism due to the variable range hopping of polaron at low temperature can be described by the Mott's equation:[8, 66, 67]

$$\rho(T) = \rho_0 \exp[T_0 / T]^{1/4} \qquad (6)$$

where ρ_0 and T_0 are constants and are given by

$$\rho_0 = \{[8\pi \alpha k_B T / N(E_F)]^{1/2}\} / (3e^2 \nu_{ph}) \qquad (7)$$

and,

$$T_0 = 18 \alpha^3 / [k_B N(E_F)] \qquad (8)$$

where ν_{ph} ($\sim 10^{13}$ s^{-1}) is the phonon frequency at Debye temperature, $N(E_F)$ the density of localized electron states at Fermi level, and α the inverse localization length. Using Eqns. (6) and (7) a linear plot is expected from $ln(\rho T^{-1/2})$ *vs.* $(1/T)^{1/4}$ for VRH conduction. The linear fit of $ln(\rho T^{-1/2})$ *vs.* $(1/T)^{1/4}$ plot (Inset (ii) of Fig. 15) indicates that VRH is the

dominant mechanism of conduction at low temperature. We have found similar behavior for both undoped ZnO and other Fe-doped samples.

Summary and conclusions

Here we have presented the results of the extensive studies on sol–gel derived Fe-doped ZnO diluted magnetic semiconductors (DMSs) nanoparticles. The x-ray diffraction data with Rietveld refinement, HRTEM, and micro-Raman analysis show that Fe-doped ZnO nanoparticles have wurtzite structure as that of pure ZnO. Furthermore, these results indicate that Fe-ions have entered in Zn-sites by substituting the Zn ions. Crystallite structure, morphology, and size have been estimated by XRD and HRTEM. The estimated size of the crystallites decreases exponentially with the increase of Fe-concentration which is due to the difference of the ionic radii between Zn and Fe atoms. The EXAFS results show that the reduction in oxygen coordination has taken place which manifests generation of oxygen vacancies in the samples due to Fe doping. The oxygen coordination remains lower and DW factor remains higher compared to their respective values in undoped ZnO suggests that doping takes place properly throughout the whole composition range. The DW factor for the next near Zn shell shows that Fe-doping affects the O site more than the Zn/Fe site. The substitution of Zn ions by Fe ions does not cause any significant change in the host lattice as manifested in the values of the bond distances. XANES study clearly rules out the presence of metallic Fe clusters, FeO and Fe_2O_3 phases in the samples. However it indicates that Fe gets incorporated in the ZnO lattice as Fe^{+3} causing creation of oxygen vacancies. These observations corroborate to those of EXAFS study. Raman study reveals that the local symmetry in the Fe-doped nanocrystals gradually differ from that of undoped sample, but the crystal structure remains the same as that of the wurtzite structure of pure ZnO; which further supports the incorporation of Fe-ions in the ZnO lattice. Room temperature (weak) ferromagnetism (RTFM) is observed from M-H measurements and magnetization increases with increasing Fe-concentration. The joint effects of the intrinsic exchange interactions arising from oxygen vacancy assisted bound magnetic polarons (BMPs) and the extrinsic grain boundary are responsible for the room temperature FM in this system. Temperature variation of resistivity measurements show two types of conduction mechanism viz.

thermally activated conduction (Arrhenius) mechanism is valid in the high temperature region and Mott's variable-range hopping (VRH) mechanism is valid in low temperature region for low Fe-concentrations ($0 \leq x \leq 0.02$) where only thermally activated conduction (Arrhenius) mechanism is observed for high Fe-concentrations ($x \geq 0.04$).

Acknowledgements

References

1   Furdyna, J. K.; Kossut, J. *Eds.: Diluted Magnetic Semiconductors, (Semiconductors and Semimetals);* Academic Press, New York,1988, Vol. **25**.

2   S. A. Wolf, D. D. Awschalom, R. A. Buhrman, J. M. Daughton, S. von Molnar, M. L. Roukes, A. Y. Chtchelkanova and D. M. Treger, *Science*, 2001, **294**, 1488-1495.

3   Y. Ohno, D. K. Young, B. Beschoten, F. Matsukura, H. Ohno and D. D. Awschalom, *Nature*, 1999, **402**, 790-792.

4   I. Djerdj, G. Garnweitner, D. Arcon, M. Pregelj, Z. Jaglicic and M. Niederberger, *J. Mater. Chem*., 2008, **18**, 5208-5217.

5   J. Chaboy, R. Boada, C. Piquer, M. A. Laguna-Marco, M. García-Hernández, N. Carmona, J. Llopis, M. L. Ruíz-González, J. González-Calbet, J. F. Fernández and M. A. García, *Phys. Rev. B:Condens. Matter Mater.Phys.*, 2010, **82**, 064411.

6   I. Balti, A. Mezni, A. Dakhlaoui-Omrani, P. Leone, B. Viana, O. Brinza, L. S. Smiri and N. Jouini, *J. Phys. Chem. C*, 2011, **115**, 15758-15766.

7   I. Bilecka, L. Luo, I. Djerdj, M. D. Rossell, M. Jagodic, Z. Jaglicic, Y. Masubuchi, S. Kikkawa and M. Niederberger, *J. Phys. Chem. C*, 2011, **115**, 1484–1495.

8   S. Kumar, S. Basu, B. Rana, A. Barman, S. Chatterjee, S. N. Jha, D. Bhattacharyya, N. K. Sahoo and A. K. Ghosh, *J. Mater. Chem. C*, 2014, **2**, 481-495.

9   S. Kumar, S. Mukherjee, R. K. Singh, S. Chatterjee and A. K. Ghosh, *J. Appl. Phys.*, 2011, **110**, 103508.

10   B. Panigrahy, M. Aslam and D. Bahadur, *Nanotechnology*, 2012, **23**, 115601.

11   J. A. Sans, J. F. Sánchez-Royo, A. Segura, G. Tobias and E. Canadell, *Phys. Rev. B: Condens. Matter Mater. Phys.*, 2009, **79**, 195105.

12   S. Kumar, S. Chatterjee, K. K. Chattopadhyay and A. K. Ghosh, *J. Phys. Chem. C*, 2012, **116**, 16700−16708.

13   S. J. Pearton, C. R. Abernathy, M. E. Overberg, G. T. Thaler, D. P. Norton, N. Theodoropoulou, A. F. Hebard, Y. D. Park, F. Ren, J. Kim and L. A. Boatner, *J. Appl. Phys.*, 2003, **93**, 1.

14   K. C. Sebastian, M. Chawda, L. Jonny and D. Bodas, *Mater. Lett.*, 2010, **64**, 2269-2272.

15   T. Dietl, H. Ohno, F. Matsukura, J. Cibert and D. Ferrand, *Science*, 2000, **287**, 1019-1022.

16   K. Sato and H. K. Yoshida, *Jpn. J. Appl. Phys.*, 2000, **39 (Part 2)**, L555-L558.

17   T. Tamura and H. Ozaki, *J. Phys.: Condens. Matter*, 2009, **21**, 026009.

18   A. Singhal, S. N. Achary, A. K. Tyagi, P. K. Manna and S. M. Yusuf, *Mater. Sci. Eng. B* 2008, **47**, 153.

19   S. Kumar, Y. J. Kim, B. H. Koo, S. K. Sharma, J. M. Vargas, M. Knobel, S. Gautam, K. H. Chae, D. K. Kim, Y. K. Kim and C. G. Lee, *J. Appl. Phys.*, 2009, **105**, 07C520.

20   A. K. Mishra and D. Das, *Mater. Sci. Eng.*, B 2010, **171**, 5-10.

21   M. Venkatesan, C. B. Fitzgerald, J. G. Lunney and J. M. D. Coey, *Phys. Rev. Lett.*, 2004, **93**,177206.

22   J. B. Goodenough, *Magnetism and the Chemical Bonds*, New York: Inter science Publishers, 1963.

23   B. B. Straumal, A. A. Mazilkin, S. G. Protasova, P. B. Straumal, A. A. Myatiev, G. Schütz, E. J. Goering, T. Tietze and B. Baretzky, *Philos. Mag.*, 2013, **93**, 1371-1383.

24   B. B. Straumal, S. G. Protasova, A. A. Mazilkin, G. Schütz, E. Goering, B. Baretzky and P. B. Straumal, *JETP Letters*, 2013, **97**, 367-377.

25   X. Gao, Y. Cui, R. M. Levenson, L. W. K. Chung and S. Nie, *Nat. Bio-technol.*, 2004, **22**, 969-976.

26   T. L. Doane and C. Burda, *Chem. Soc. Rev.*, 2012, **41**, 2885-2911.

27   H. M. Xiong, *Adv. Mater.*, 2013, **25**, 5329–5335.

28   A. K. Zak, W. H. A. Majid, M. E. Abrishami and R. Yousefi, *Solid State Sci.*, 2011, **13**, 251-256.

29   S. J. Han, J. W. Song, C. H. Yang, S. H. Park, J. H. Park, Y. H. Jeong and K. W. Rhie, *Appl. Phys. Lett.*, 2002, **81**, 4212-4214.

30   D. Karmakar, S. K. Mandal, R. M. Kadam, P. L. Paulose, A. K. Rajarajan, T. K. Nath, A. K. Das, I. Dasgupta and G. P. Das, *Phys. Rev. B: Condens. Matter Mater. Phys.*, 2007, **75**, 144404.

31   J. Anghel, A. Thurber, D. A. Tenne, C. B. Hanna and A. Punnoose, *J. Appl. Phys.*, 2010, **107**, 09E314.

32   R. Saleh, S. P. Prakoso and A. Fishli, *J. Magn. Magn. Mater.*, 2012, **324**, 665-670.

33   H. Morkoç, Ü. Özgür, *Zinc Oxide- Fundamentals, Materials and Device Technology*, WILEY-VCH Verlag GmbH, Germany, 2009.

34   Ü. Özgür, Y. I. Alivov, C. Liu, A. Teke, M. A. Reshchikov, S. Doğan, V. Avrutin, S.-J. Cho and H. Morkoç, *J. Appl. Phys.*, 2005, **98**, 041301.

35   M. Gaudon, O. Toulemonde and A. Demourgues, *Inorg. Chem.*, 2007, **46**, 10996-11002.

36   J. Luo, J. K. Liang, Q. L. Liu, F. S. Liu, Y. Zhang, B. J. Sun and G. H. Rao, *J. Appl. Phys.*, 2005, **97**, 086106.

37   G. K. Williamson and W. H. Hall, *Acta Metall.*, 1953, **1**, 22-31.

38   E. Prince, J. K. Stalick, *Accuracy in Powder Diffraction II, NIST Special Publication*, Vol. **597**, 1992.

39   S. Basu, S. Varma, A. N. Shirsat, B. N. Wani, S. R. Bharadwaj, A. Chakrabarti, S. N. Jha and D. Bhattacharrya, *J. Appl. Phys.*, 2013, **113**, 043508.

40   S. Basu, D. K. Patel, J. Nuwad, V. Sudarsan, S. N. Jha, D. Bhattacharyya, R. K. Vatsa and S. K. Kulshreshtha, *Chem. Phys. Lett.*, 2013, **561-562**, 82-86.

41   M. Walter, J. Somers, A. Fernandez, E. D. Specht, J. D. Hunn, P. Boulet, M. A. Denecke and C. Gobel, *J. Mater Sci.*, 2007, **42**, 4650-4658.

42   D. C. Konigsberger and R. Prince, *X-Ray Absorption: Principles, Applications, Techniques of EXAFS, SEXAFS and XANES*, Wiley, New York, 1988.

43   M. Newville, B. Ravel, D. Haskel, J. J. Rehr, E. A. Stern and Y. Yacoby, *Physica B*, 1995, **208-209**, 154-156.

44   E. H. Kisi and M. M. Elcombe, *Acta Cryst.*, 1989, **C45**, 1867-1870.

45   S. Basu, D.Y. Inamdar, S. Mahamuni, A. Chakrabarti, C. Kamal, G.R. Kumar, S.N. Jha and D. Bhattacharyya, *J. Phys. Chem. C.*, 2014, **118** (17), 9154–9164.

46   P. E. Lippens, A. V. Chadwick, A. Weibel, R. Bouchet and P. Knauth, *J. Phys. Chem. C* 2008, *112,* 43-47.

47   J. B. Wang, G. J. Huang, X. L. Zhong, L. Z. Sun, Y. C. Zhou and E. H. Liu, *Appl. Phys. Lett.*, 2006, **88**, 252502.

48   L. W. Yang, X. L. Wu, G. S. Huang, T. Qiu and Y. M. Yang, *J. Appl. Phys.*, 2005, **97**, 014308.

49   D. G. Mead and G. R. Wilkinson, *J. Raman Spectrosc.*, 1977, **6**, 123-129.

50   S. Singh and M. S. Ramachandra Rao, *Phys. Rev. B: Condens. Matter Mater. Phys.*, 2009, **80**, 045210.

51   J. M. Calleja and M. Cardona, *Phys. Rev. B: Condens. Matter Mater. Phys.*, 1977, **16**, 3753.

52   X. Wang, J. Xu, X. Yu, K. Xue, J. Yu and X. Zhao, *Appl. Phys. Lett.*, 2007, **91**, 031908.

53   T. C. Damen, S. P. S. Porto and B. Tell, *Phys. Rev.*, 1966, **142**, 570-574.

54   J. Serrano, A. H. Romero, F. J. Manjo'n, R. Lauck, M. Cardona and A. Rubio, *Phys. Rev. B: Condens. Matter Mater. Phys.*, 2004, **69**, 094306.

55   R. Cuscó, E. A. Lladó, J. Ibáñez, L. Artús, J. Jiménez, B. Wang and M. J. Callahan, *Phys. Rev. B: Condens. Matter Mater. Phys.*, 2007, **75**, 165202.

56   S. Chen, Y. Liu, C. Shao, R. Mu, Y. Lu, J. Zhang, D. Shen and X. Fan, *Adv. Mater.*, 2005, **17**, 586-590.

57   Y. J. Xing, Z. H. Xi, Z. Q. Xue, X. D. Zhang, J. H. Song, R. M. Wang, J. Xu, Y. Song, S. L. Zhang and D. P. Yu, *Appl. Phys. Lett.*, 2003, **83**, 1689-1691.

58   J. D. Ye, S. L. Gu, S. M. Zhu, S. M. Liu, Y. D. Zheng, R. Zhang, Y. Shi, Q. Chen, H. Q. Yu and Y. D. Ye, *Appl. Phys. Lett.*, 2006, **88**, 101905.

59   B. Martínez, F. Sandiumenge, Ll. Balcells, J. Arbiol, F. Sibieude and C. Monty, *Phys. Rev. B: Condens. Matter Mater. Phys.*, 2003, **72**, 165202.

60   O. D. Jayakumar, H. G. Salunke, R. M. Kadam, M. Mahapatra, G. Yashwant and S. K. Kulshreshtha, *Nanotechnology*, 2006, **17**, 1278-1285.

61   B. B. Straumal, A. A. Mazilkin, S. G. Protasova, A. A. Myatiev, P. B. Straumal, G. Schütz, P. A. V. Aken, E. Goering and B. Baretzky, *Phys. Rev. B: Condens. Matter Mater. Phys.*, 2009, **79**, 205206.

62   A. Kaminski and S. D. Sarma, *Phys. Rev. Lett.*, 2002, **88**, 247202.

63   J. M. D. Coey, M. Venkatesan and C. B. Fitzgerald, *Nat. Mater.*, 2005, **4**, 173-179.

64   S. D. Sarma, E. H. Hwang and A. Kaminski, *Phys. Rev. B: Condens. Matter Mater. Phys.*, 2003, **67**, 155201.

65   B. Pal and P. K. Giri, *J. Appl. Phys.*, 2010, **108**, 084322.

66   N. F. Mott and E. A. Davis, *Electronics Process in Non-Crystalline materials,* Clarendon, Oxford, 1979.

67   N. Sharma, S. Granville, S. C. Kashyap and J.-Ph. Ansermet, *Phys. Rev. B: Condens. Matter Mater. Phys.*, 2010, **82**, 125211.

Figure Captions:

Fig. 1 Rietveld refinement profiles of X-ray diffraction data of the $Zn_{1-x}Fe_xO$ ($0 \leq x \leq 0.06$) samples. The circle represents the observed data (Obs) while solid line through the circles is the calculated profile (Calc), vertical tics below curves represent allowed Bragg-reflections for the wurtzite phase. The difference pattern of the observed data and calculated profile (Obs−Calc) is given below the vertical tics.

Fig. 2 Variation of lattice parameter ('*a*' and '*c*') with Fe-concentration (x) calculated from Rietveld refinement. The inset (i) shows the variation of the unit cell volume and inset (ii) shows the variation of the degree of distortion (*R*).

Fig. 3 (a) Variation of average basal bond angles (O_b-Zn-O_b) and average base-apex angles (O_b-Zn-O_a) with Fe-concentration (x); (b) Variation of bond length Zn-O_a and Zn-

O_b with Fe-concentration (x). Inset of (b) shows the variations of inter planer spacing (d_{100}) with Fe-concentration (x).

Fig. 4 $(d_{hkl}\beta Cos\theta/\lambda)^2$ vs. $(d_{hkl}{}^2\beta Cos\theta/\lambda^2)$ plot of the ZnO:Fe samples to estimate crystallite size *(D)* and average strain (ε).

Fig. 5 Variation of average crystallite size with Fe-concentration (x) estimated from size-strain plot. The inset figure shows the variation of strain estimated from size-strain plot.

Fig. 6 Low magnification TEM (a), HRTEM (b), and SAED (c) images of ZnO nanocrystals and low magnification TEM (d), HRTEM (e), and SAED (f) images of $Zn_{0.99}Fe_{0.02}O$ nanocrystals.
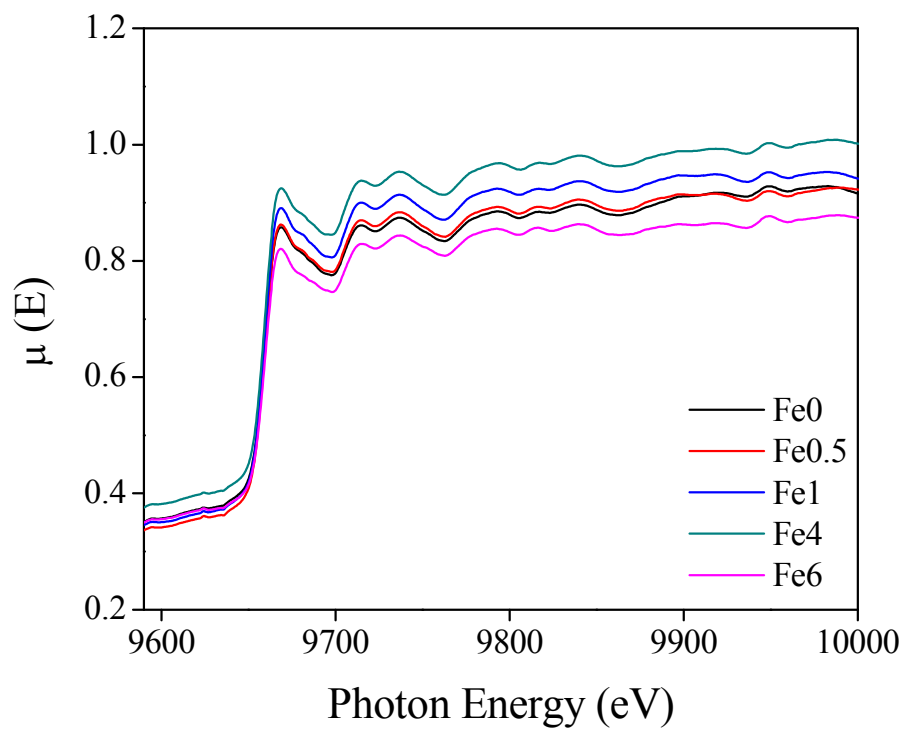
Fig. 7 Normalized experimental EXAFS ($\mu(E)$ vs E) for undoped and Fe doped ZnO nanocrystals at Zn K-edge.

Fig. 8 FT-EXAFS ($\chi(R)$ *vs R*) for undoped and Fe doped ZnO nanocrystals at Zn K-edge.

Fig. 9 Variation of bond lengths of Zn-O shells and Zn-Zn shells with change in doping concentration.

Fig. 10 Variation of total coordination number of Zn-O shells and Zn-Zn shells with change in doping concentration

Fig. 11 Variation of Debye-Waller factor of nearest Zn–O shell and next nearest Zn–Zn shell with change in dopant concentration.

Fig. 12 XANES spectrum of Fe doped ZnO nanocrystals along with that of Fe metal foil and standard Fe_2O_3 and FeO samples.

Fig. 13 Room-temperature Raman spectra of $Zn_{1-x}Fe_xO$ ($0\leq x\leq0.06$) nanoparticles. Inset of figure shows the variation of the (E_{2H}) peak with Fe-concentration (x) with respect to its pure ZnO value (curve-I) and the variation of the $2(E_{2H} - E_{2L})$ peak value with x with respect to its corresponding ($E_{2H} - E_{2L}$) peak value (curve-II).

Fig. 14 Room temperature M-H curves of the $Zn_{1-x}Fe_xO$ ($0\leq x \leq 0.06$) samples. Inset figure shows the enlarged view of Fe0 (ZnO) and Fe2 samples.

Fig.15 Variation of resistivity (ρ) with temperature (T) for Fe0, Fe0.5 and Fe1.5 samples. Inset figure (i) shows $\ln\rho$ vs. 1000/T plot. The liner fit shows that the thermal activation is valid at high temperature region. Inset figure (ii) shows the variation of $\ln(\rho T^{-1/2})$ with $T^{-1/4}$ for Fe0.5 and Fe1.5 samples. The linear fit indicates that the variable range hopping conduction is active in this (low) temperature range.

TOC

XANES study at Fe edge (a) and signature of ferromagnetism (b) of Zn1-xFexO nanoparticles.

TABLES:

Table 1. Values of lattice parameters, bond lengths and bond angles calculated following ref. 35

Table 2. Crystallite size and average strain estimated from Williamson–Hall plot.

Table 3. Observed Raman peaks of $Zn_{1-x}Fe_xO$ ($0 \leq x \leq 0.06$) nanoparticles and their assignments.

Table 4. Estimated activation energy (E_a) of $Zn_{1-x}Fe_xO$ (x= 0, 0.005, 0.01 and 0.04).

Table 1. Values of lattice parameters, bond lengths and bond angles:

Parameters	Fe0	Fe0.5	Fe1	Fe1.5	Fe2	Fe4	Fe6
a (Å)	3.24564	3.24546	3.24550	3.24579	3.24581	3.24586	3.24560
c (Å)	5.19985	5.19982	5.19982	5.19982	5.19985	5.2001	5.20010
c/a	1.60210	1.60218	1.60217	1.60202	1.60202	1.60207	1.60219
u	0.37986	0.37985	0.37985	0.37988	0.37988	0.37987	0.37985
d_{Zn-O_a} (Å)	1.97521	1.97515	1.97518	1.97530	1.97532	1.97537	1.97526
d_{Zn-O_b} (Å)	1.97526	1.97517	1.97519	1.97531	1.97532	1.97538	1.97527
O_a-Zn-O_b (°)	108.43732	108.43960	108.43939	108.43356	108.43356	108.43556	108.43980
O_b-Zn-O_b (°)	110.48503	110.48283	110.48304	110.48874	110.48864	110.48673	110.48271

Table 2. Crystallite size and average strain estimated from Williamson–Hall and Size-Strain plot.

Sample	Particle Size (nm)			Strain	
	Scherrer formula	Size-Strain Plot	W-H Plot	Size-Strain Plot	W-H Plot
Fe0	32	34	33	2.9×10^{-4}	4.9×10^{-5}
Fe0.5	25	29	30	3.5×10^{-3}	3.9×10^{-4}
Fe1	22	25	25	4.0×10^{-3}	3.8×10^{-4}
Fe1.5	21	24	26	4.7×10^{-3}	6.4×10^{-4}
Fe2	18	23	25	8.4×10^{-3}	1.3×10^{-3}
Fe4	15	17	20	6.0×10^{-3}	1.2×10^{-3}
Fe6	14	16	20	14.0×10^{-3}	2.7×10^{-3}

Table 3. Observed Raman peaks of $Zn_{1-x}Fe_xO$ ($0 \leq x \leq 0.06$) nanoparticles and their symmetry assignments.

Vibration frequency (cm^{-1})							Assignments	Process
Fe0	**Fe0.5**	**Fe1**	**Fe1.5**	**Fe2**	**Fe4**	**Fe6**		
329	328	327	327	327	328	329	E_{2H}-E_{2L}	Second order
378	379	378	380	380	398	398	A_1(TO)	First order
408	----	----	----	----	----	----	E_1(TO)	First order
434	435	435	435	434	434	434	E_{2H}	First order
575	576	579	577	575	574	574	A_1(LO)	First order
585	----	----	----	----	----	----	E_1(LO)	First order
658	658	659	659	659	680	680	$2(E_{2H}$-$E_{2L})$	Second order of $(E_{2H}$-$E_{2L})$
1142	1124	1150	1144	1147	1120	1120	$2[A_1$(LO)]	Second order of A_1(LO)

Table 4. Variation of activation energy (E_a) of $Zn_{1-x}Fe_xO$ (x= 0, 0.005, 0.015 and 0.04).

Sample	Activation energy E_a (eV)
Fe0	0.233 ± 0.019
Fe0.5	0.347 ± 0.007
Fe1.5	0.394 ± 0.007
Fe4	0.376 ± 0.011

Fig. 1 Rietveld refinement profiles of X-ray diffraction data of the $Zn_{1-x}Fe_xO$ ($0 \leq x \leq 0.06$) samples. The circle represents the observed data (Obs) while solid line through the circles is the calculated profile (Calc), vertical tics below curves represent allowed

Bragg-reflections for the wurtzite phase. The difference pattern of the observed data and calculated profile (Obs−Calc) is given below the vertical tics.

Fig. 2 Variation of lattice parameter ('*a*' and '*c*') with Fe-concentration (x) calculated from Rietveld refinement. The inset (i) shows the variation of the unit cell volume and inset (ii) shows the variation of the degree of distortion (*R*).

Fig. 3 (a) Variation of average basal bond angles (O_b-Zn-O_b) and average base-apex angles (O_b-Zn-O_a) with Fe-concentration (x); (b) Variation of bond length Zn-O_a and Zn-O_b with Fe-concentration (x). Inset of (b) shows the variations of inter planer spacing (d_{100}) with Fe-concentration (x).

Fig. 4 $(d_{hkl}\beta Cos\theta/\lambda)^2$ vs. $(d_{hkl}{}^2\beta Cos\theta/\lambda^2)$ plot of the ZnO:Fe samples to estimate crystallite size *(D)* and average strain (ε).

Fig. 5 Variation of average crystallite size with Fe-concentration (x) estimated from size-strain plot. The inset figure shows the variation of strain estimated from size-strain plot.

30

Fig. 6 Low magnification TEM (a), HRTEM (b), and SAED (c) images of ZnO nanocrystals and low magnification TEM (d), HRTEM (e), and SAED (f) images of $Zn_{0.99}Fe_{0.02}O$ nanocrystals.

Fig. 7 Normalized experimental EXAFS (μ(E) vs E) for undoped and Fe doped ZnO nanocrystals at Zn K-edge.

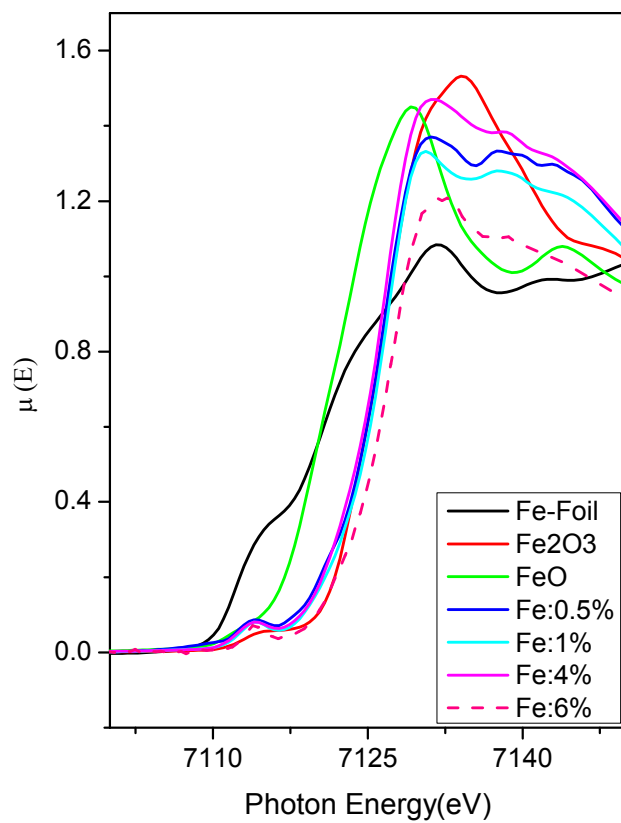**Fig. 8** FT-EXAFS ($\chi(R)$ *vs R*) for undoped and Fe doped ZnO nanocrystals at Zn K-edge.

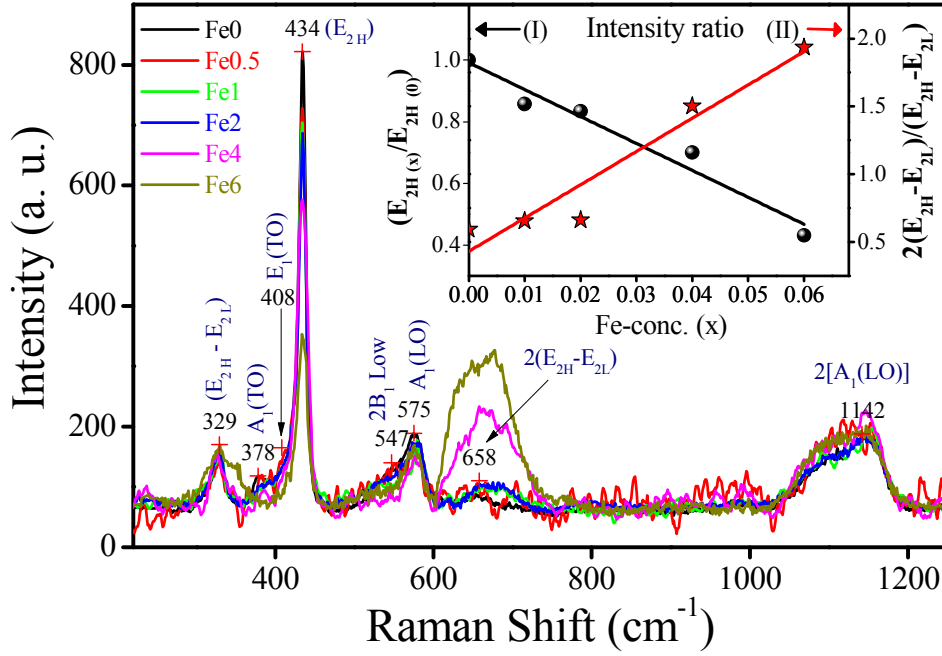**Fig. 9** Variation of bond lengths of Zn-O shells and Zn-Zn shells with change in doping concentration.

Fig. 10 Variation of total coordination number of Zn-O shells and Zn-Zn shells with change in doping concentration.
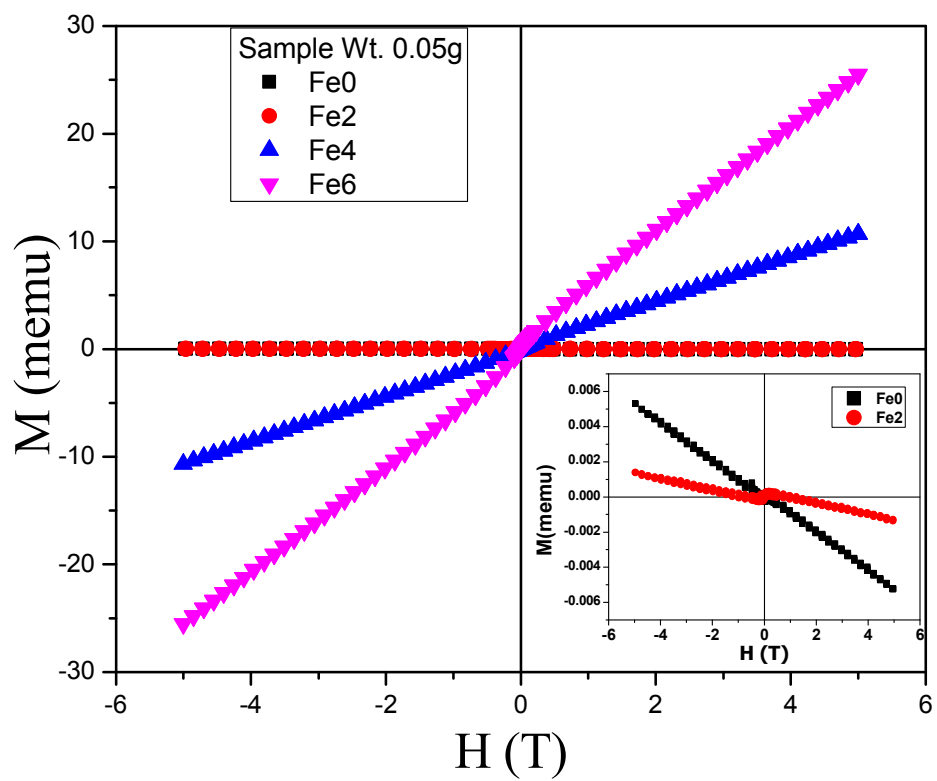
Fig. 11 Variation of Debye-Waller factor of Zn-O shells and Zn-Zn shells with change in doping concentration.
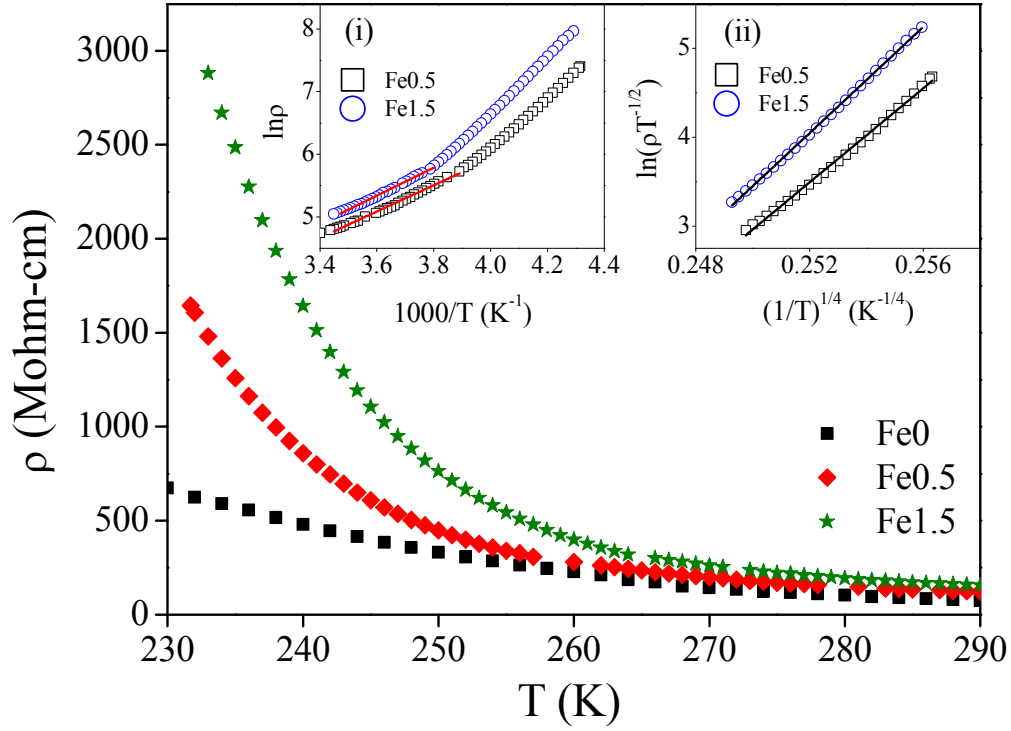
Fig. 12 XANES spectrum of Fe doped ZnO nanocrystals along with that of Fe metal foil and standard Fe_2O_3 and FeO samples.

Fig. 13 Room-temperature Raman spectra of $Zn_{1-x}Fe_xO$ ($0 \leq x \leq 0.06$) nanoparticles. Inset of figure shows the variation of the (E_{2H}) peak with Fe-concentration (x) with respect to its pure ZnO value. The inset shows the variation of the ratios $E_{2H(x)}/E_{2H(0)}$ (curve I) and $2(E_{2H} - E_{2L})/(E_{2H} - E_{2L})$ (curve-II) with x respectively .
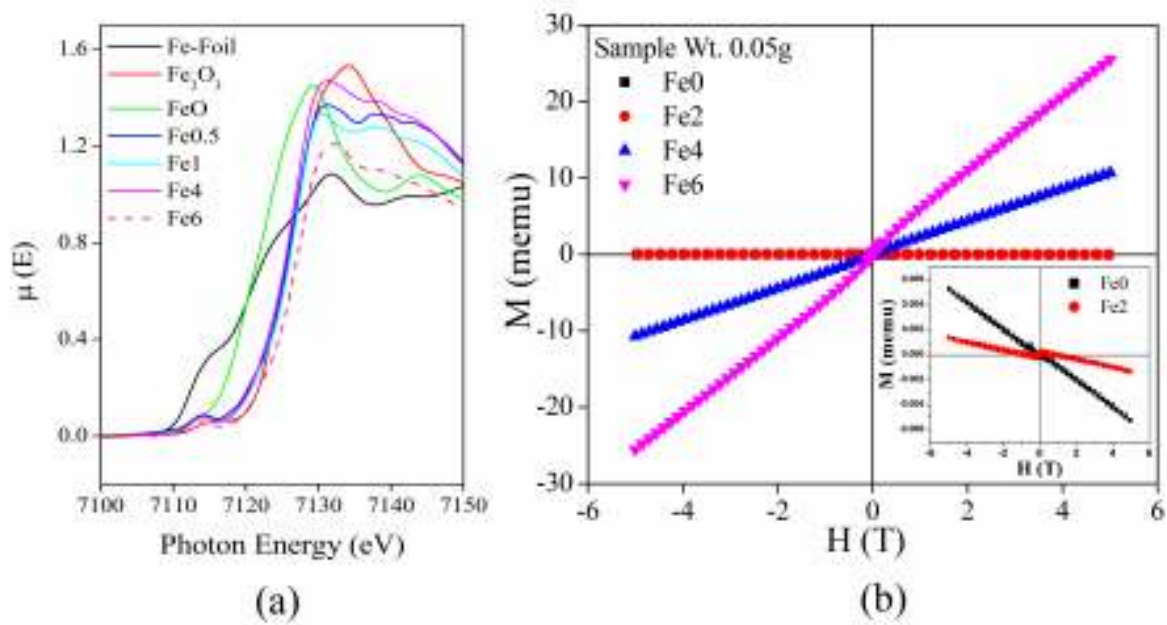
Fig. 14 Room temperature M-H curves of the $Zn_{1-x}Fe_xO$ ($0 \leq x \leq 0.06$) samples. Inset figure shows the enlarged view of Fe0 (ZnO) and Fe2 samples.

Fig. 15 Variation of resistivity (ρ) with temperature (T) for Fe0, Fe0.5 and Fe1.5 samples. Inset figure (i) shows $\ln\rho$ vs. 1000/T plot. The liner fit shows that the thermal activation is valid at high temperature region. Inset figure (ii) shows the variation of $\ln(\rho T^{-1/2})$ with $T^{-1/4}$ for Fe0.5 and Fe1.5 samples. The linear fit indicates that the variable range hopping conduction is active in this (low) temperature range.

(a)

(b)

TOC

XANES study at Fe edge (a) and signature of ferromagnetism (b) of Zn1-xFexO nanoparticles.